

Thermal stability of a nanocrystalline HfNbTiZr multi-principal element alloy processed by high-pressure torsion



Pham Tran Hung^a, Megumi Kawasaki^b, Jae-Kyung Han^b, János L. Lábár^{a,c}, Jenő Gubicza^{a,*}

^a Department of Materials Physics, Eötvös Loránd University, Budapest H-1518, P.O.B. 32, Hungary

^b School of Mechanical, Industrial and Manufacturing Engineering, Oregon State University, Corvallis, OR 97331, USA

^c Institute for Technical Physics and Materials Science, Centre for Energy Research, Budapest, Hungary

ARTICLE INFO

Keywords:

Multi-principal element alloy
Severe plastic deformation
Microstructure
Thermal stability
Recovery
Hardness

ABSTRACT

The microstructural stability of a nanocrystalline HfNbTiZr multi-principal element alloy was studied by annealing the material in a differential scanning calorimeter (DSC). The as-received sample was obtained by severe plastic deformation using the high-pressure torsion (HPT) technique. Samples were annealed to the characteristic temperatures of the DSC thermogram, namely up to 740, 890 and 1000 K, and the microstructure of the heat treated specimens was analyzed. It was found that the heating up to 740 K yielded a decomposition of the initial body-centered cubic (bcc) phase into two bcc phases with a lower and a higher lattice constant. During annealing up to 890 K, a Zr/Hf-rich hexagonal-close packed (hcp) phase started to nucleate. Heating the sample up to 1000 K resulted in the formation of a nanocrystalline Zr/Hf-rich bcc phase beside the Zr/Hf-rich hcp and the Nb-rich bcc phases. Beside the phase transformation a recovery of the severely deformed defect structure and a grain coarsening were also observed which was accompanied by a reduction of the hardness above 740 K.

1. Introduction

Since first reported in 2004, multi-principal element alloys (MPEAs) including high-entropy alloys (HEAs) [1,2], which are composed of multiple principal elements in equal or near equal molar ratios, have received a great deal of attention from the scientific community [3]. This is not only due to the vast amount of new materials, but also thanks to their outstanding and unique properties, such as high ductility at cryogenic temperatures [4], good wear resistance [5], and superconductivity [6]. Out of these new materials, refractory MPEAs are among the most suitable for high temperature applications. These MPEAs are based on refractory elements (consisting of nine elements in Group IV (Ti, Zr, Hf), Group V (V, Nb, Ta), and Group VI (Cr, Mo, W)), all of which have melting points higher than 1875 °C. Since it is known that alloys generally maintain their strength at temperatures below ~0.6 of their absolute melting temperature, refractory alloys are employable at higher temperatures than other metallic materials. However, even though many refractory MPEAs exhibit high temperature strength, most of them are rather brittle at room temperature [7]. One of the alloys that was reported to exhibit both high hardness at elevated temperature and good ductility at room temperature is the equimolar refractory MPEA HfNbTiZr [8]. Therefore, the present study focuses on this material.

Other than chemical composition, the mechanical properties of metallic materials can be tuned using severe plastic deformation (SPD). A material after processing by SPD has an increased lattice defect density (e.g. dislocation density or twin fault probability) and a decreased grain size, resulting in a considerable strength enhancement. In a previous report [9], it was shown that HfNbTiZr after processing by 10 turns of high-pressure torsion (HPT) has a reduced grain size to the nanocrystalline regime and a large dislocation density of $\sim 210 \times 10^{14} \text{ m}^{-2}$, thereby exhibiting an outstanding hardness of about 4400 MPa. Haché et al. has summarized that generally, nanocrystalline MPEAs surpass coarse-grained MPEAs and nanocrystalline conventional alloys in strength, while exhibiting higher thermal stability than pure and binary nanocrystalline materials [10]. Hence HPT is the treatment of choice in this paper.

One key feature of MPEAs is their high-entropy configuration, which is maximized when the material is in one solid solution phase. However, it was found that a number of MPEAs decomposed when exposed to elevated temperatures. For example, CoCrFeMnNi formed three distinct phases after prolonged exposure at 500 °C [11], or in AlTiVNb processed by HPT, intermetallic phases precipitated after annealing [12]. This phase separation is found to be heavily dependent on the material chemical composition. In the case of CoCrFeMnNi alloy, several investigations have been conducted on the effect of Co, Mn and

* Corresponding author.

E-mail address: jeno.gubicza@ttk.elte.hu (J. Gubicza).

Ni on the phase stability [13–15], showing the stabilizing/destabilizing effect of different elements on different phases. Similar researches have also been done for other alloys [16,17]. Nevertheless, it is possible for the phase decomposition to be beneficial to the mechanical properties of the materials, as shown for e.g., the AlTiVNb MPEA, where its hardness increased when the MPEA was annealed up to 700 °C, while decreased at higher temperatures. Such unusual anneal response was also observed in other nanocrystalline MPEAs [18,19]. Other behaviours after annealing were also observed. For example, HfNbTaTiZr after being brought to elevated temperatures (600, 800 and 1000 °C) was initially hardened; however, as the holding time increased, the material hardness declined [20].

In this paper, the thermal stability of a nanocrystalline HfNbTiZr MPEA is investigated. The nanostructured microstructure was achieved by 10 turns of HPT. First, the characteristic temperatures for the evolution of the nanostructure are determined by calorimetry. Then, samples are heated up to these temperatures, and the microstructure and the phase composition in the annealed specimens are characterized in detail. Finally, the effect of these changes on the hardness is revealed.

2. Material and methods

2.1. Processing of the material

Magnetic levitation melting of a mixture of four pure components (purity > 99.9 wt%) was used for synthesizing the Hf₂₅Nb₂₅Ti₂₅Zr₂₅ MPEA, followed by the homogenization heat treatment at 1290 °C for 24 h. The cast material was machined into cylindrical billets with a diameter of 10 mm, and these billets were sliced by electric discharge machining (EDM) into disks with a thickness of ~1 mm. The final disk thickness of ~0.85 mm was achieved by mechanical grinding. A conventional HPT facility with quasi-constrained set-up was utilized for the HPT process [21]. The HPT processing was conducted for 10 turns at room temperature under a pressure of 6.0 GPa at a rotational speed of 1 rpm.

2.2. Differential scanning calorimetry

The thermal stability of the nanocrystalline HfNbTiZr MPEA material was studied on the disk edges subjected to 10 turns by HPT. Specifically, small specimens with a width of about 1 mm were cut from the HPT-processed disk using a diamond saw, therefore the characterization was conducted at the HPT disk edges between the radii of 4 and 5 mm. These specimens were subjected to annealing in a differential scanning calorimetry (DSC) using a Perkin Elmer (DSC2) calorimeter. First, a sample was heated up to the maximum test temperature, 1000 K at a heating rate of 40 K/min under an Ar atmosphere. Then, the characteristic temperatures of the microstructure evolution were determined from the thermogram. Finally, individual samples were heated up to these temperatures at a heating rate of 40 K/min and then quenched to room temperature at a rate of about 300 K/min for microstructure investigation.

2.3. Microstructure studied by electron microscopy

The microstructures of the HPT-processed and the annealed samples were characterized by transmission electron microscopy (TEM). Thin TEM-lamellae were prepared from the disk samples by a focused ion beam (FIB) technique using Ga⁺ ions. First, the samples were glued using a special glue at 100 °C for not more than 1 min to a Cu-stub for mechanical grinding and polishing. In the second step, ion-beam thinning of the 50 µm thick lamella was started at 7 keV using 2 mA ion current. Finally, the perforated lamella was cleaned at 3 keV and later at 1 keV from both sides to remove the damaged layers from its surfaces.

A Titan Themis G2 200 scanning transmission electron microscope

(STEM) was used for TEM and energy-disperse X-ray spectroscopy (EDS) investigations. The microscope was equipped with a four-segment Super-X EDS detector. A corrector for the spherical aberration (C_s) was applied at the imaging part, while probe-correction was not used. The image resolution is 0.16 nm in STEM Z-contrast imaging mode (recorded with a Fishione high-angle annular dark-field (HAADF) detector). The EDS data were recorded (together with the HAADF signal) in spectrum-image mode, and elemental maps were made for the constituents of the alloy in order to investigate the decomposition of the studied MPEA.

2.4. Microstructure characterization by X-ray diffraction

The phase composition was analyzed by X-ray diffraction (XRD) by utilizing a Rigaku Smartlab powder diffractometer using CuK α radiation (wavelength: $\lambda = 0.15418$ nm). Before XRD measurements, the surfaces of the samples were mechanical polished using 800, 1000, 1200, 2500 and 4000 grit papers, and subsequently colloidal silica suspension with 1 µm particle size. Then, etching was applied on the surface for ~30 s with a solution of 45 ml distilled water, 5 ml HF and 2 ml nitric acid. The lattice parameter was calculated using the Nelson-Riley method [22] applied to the diffraction peak positions.

The microstructure of the MPEA samples was investigated using X-ray line profile analysis (XLPA). The measurement of the X-ray line profiles was carried out using a high-resolution rotating anode diffractometer (type: RA-MultiMax9, manufacturer: Rigaku) with CuK α_1 radiation (wavelength: $\lambda = 0.15406$ nm). X-rays scattered into Debye-Scherrer rings were detected using two-dimensional imaging plates, and the intensity distribution perpendicular to the rings were measured as the diffraction profile. The line profiles evaluation was carried out using the Convolutional Multiple Whole Profile (CMWP) fitting method [23]. In this procedure, a fitting of all measured diffraction peaks was performed with a convolution of theoretical profiles related to diffraction domain size and dislocation density. The dependence of dislocation broadening of the diffraction peaks on the indices of reflections was taken into account by the dislocation contrast factors [23]. For cubic crystals, the contrast factors depend on two parameters, \bar{C}_{h00} and q . For Hf₂₅Nb₂₅Ti₂₅Zr₂₅ MPEA with a bcc structure, the value of \bar{C}_{h00} is about 0.31 for both edge and screw dislocations as determined in a former study [9]. The values of q are 1.5 and 2.7 for edge and screw dislocations, respectively.

2.5. Hardness test

Hardness testing was performed on the HPT-processed and the annealed samples by a Zwick Roell ZH μ indentation machine having a Vickers indenter, with 500 g applied load and 10 s dwell time. The surface before hardness testing was treated with the same manner as for XRD measurements (see Section 2.4). The average microhardness of each sample was determined from 10 measurements.

3. Results

3.1. DSC scan on the MPEA sample processed by HPT

Fig. 1 shows the DSC curve obtained for the HPT-processed HfNbTiZr MPEA at a heating rate of 40 K/min. The thermogram consists of three broad and strongly overlapping exothermic peaks. The first peak starts at 400 K and finishes at about 740 K. The second peak ends at 890 K, and there is a third smaller peak between 890 and 1000 K. These peaks may be related to the recovery/recrystallization of the HPT-processed nanocrystalline microstructure and/or phase transformations in the MPEA sample.

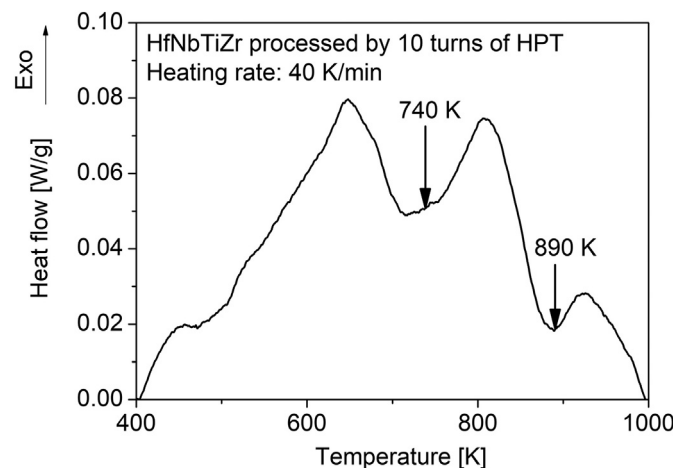


Fig. 1. DSC thermogram obtained for the sample cut from the edge of a disk processed by 10 turns of HPT.

3.2. XRD study of the evolution of phase composition during annealing

The evolution of the phase composition during annealing was studied for the nanocrystalline HfNbTiZr MPEA by XRD. The initial HPT-processed state has a single-phase bcc structure as revealed by the XRD pattern in Fig. 2 which was taken from the disk edge. The lattice constant determined from the peak positions was 0.3438 ± 0.0003 nm. The evolution of the phase composition due to heating up to different characteristic temperatures defined in the DSC curve in Fig. 1 is illustrated in the XRD profiles as shown in Fig. 3. In this figure, only a part of the diffractograms taken for the diffraction angles between 62 and 72° is shown in order to reveal the special shape of the bcc peak with the indices 211. Indeed, after annealing up to 740 K, an additional shoulder appeared at the left side of the main bcc peak. At the same time, the main bcc peak shifted to a higher angle compared to the HPT-processed state, suggesting a decrease of the lattice constant. Assuming that the bcc peak comprises two subprofiles, two Lorentzian functions were fitted to the whole reflection which gave the positions and the intensities of the two profile components. The same procedure was applied for the other bcc peaks in the pattern profile and from the subprofile positions the lattice constants of the bcc phases corresponding to the two subreflections were determined. Table 1 shows that the lattice parameter of the bcc phase corresponding to the subprofiles appeared at lower angles was 0.3485 ± 0.0007 nm. This phase is

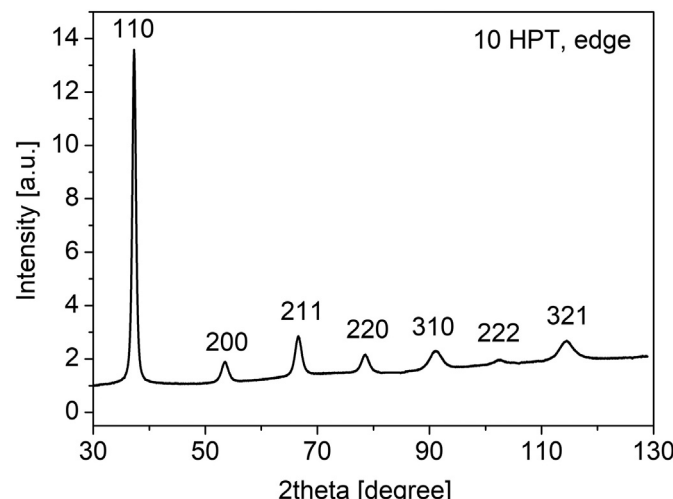


Fig. 2. XRD diffractogram for the sample cut from the edge of a disk processed by 10 turns of HPT.

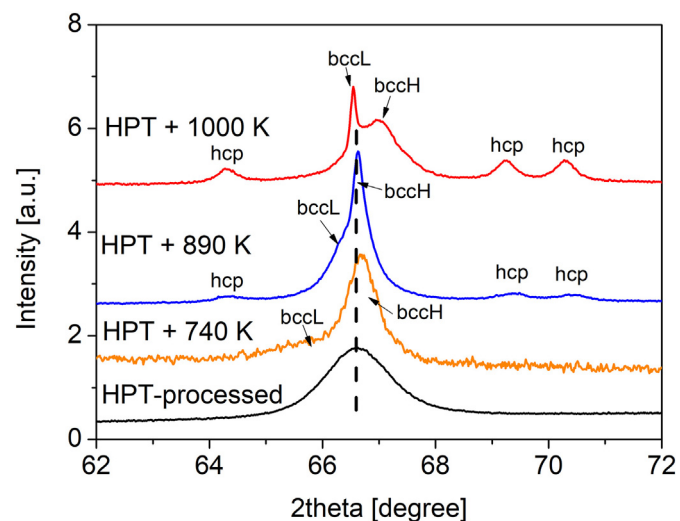


Fig. 3. Parts of the XRD patterns measured for the HPT-processed sample and the specimens annealed after HPT up to the temperatures of 740, 890 and 1000 K.

Table 1

The crystalline phases, their lattice constants and intensity fractions as obtained by XRD. BccL and bccH indicate the bcc phases for which the XRD peaks appeared at lower and higher diffraction angles, respectively (see Fig. 3).

State of material	Phases	Lattice constant [nm]	Fraction [%]
10 HPT	bcc	$a = 0.3438 \pm 0.0003$	100
10 HPT + 740 K	bccL	$a = 0.3485 \pm 0.0007$	29
	bccH	$a = 0.3427 \pm 0.0001$	71
10 HPT + 890 K	bccL	$a = 0.3443 \pm 0.0002$	41
	bccH	$a = 0.3435 \pm 0.0001$	54
	hcp	n.a.	5
10 HPT + 1000 K	bccL	$a = 0.3438 \pm 0.0001$	28
	bccH	$a = 0.3416 \pm 0.0003$	60
	hcp	$a = 0.3201 \pm 0.0002$	12
	c	$c = 0.5094 \pm 0.0003$	

denoted as bccL. For the other bcc phase scattering X-rays into higher angles (bccH), the lattice constant was obtained as 0.3427 ± 0.0001 nm. The intensity fractions of the bccL and bccH phases were 29 and 71%, respectively.

Fig. 3 shows that after annealing up to 890 K the microstructure also contained two bcc components but their lattice constants are closer than for the sample heated up to 740 K (see Table 1). The fractions of bccL and bccH phases were 41 and 54%, respectively. In addition to the bcc phases, a novel hcp phase formed while the intensity fraction was only $\sim 5\%$. Due to this low fraction of the phase, the XRD peaks were noisy and therefore the lattice constants of the hcp phase were not determined. After annealing up to 1000 K, the fraction of the hcp phase increased to about 12% and the lattice constants were obtained as $a = 0.3201 \pm 0.0002$ nm and $c = 0.5094 \pm 0.0003$ nm. Considering the similar hcp peak positions at both 890 and 1000 K, the lattice parameters at 890 K are anticipated to be consistent with the values determined for 1000 K. At the highest annealing temperature, the bcc peaks again consisted of two components: a narrow subprofile at lower diffraction angle and a much broader subreflection at higher angle. The latter profile overlapped not only with the peak bccL phase but also with the reflections of the hcp phase as shown in Fig. 4 where Lorentzian functions were fitted to the bcc and hcp peaks. The lattice parameters and the fraction of the different phases were determined from the peak positions and areas obtained for all separated peaks in the pattern. The lattice constants of the bccL and bccH phases were 0.3438 ± 0.0001 nm and 0.3416 ± 0.0003 nm, respectively. The fraction of the bccL component was $\sim 28\%$ while the major component

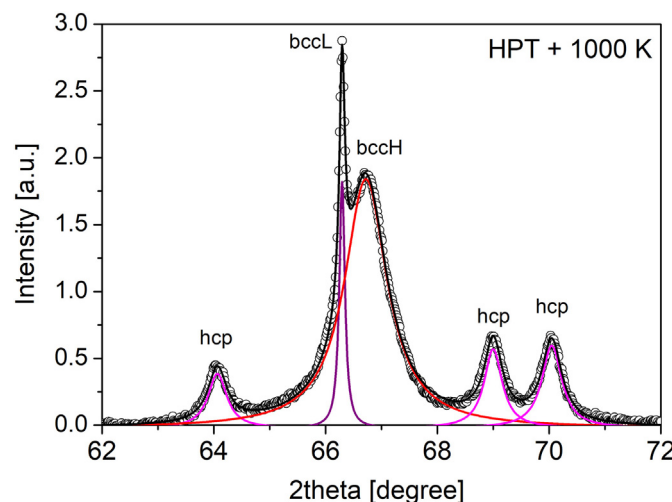


Fig. 4. Separation of the overlapping XRD peaks for the determination of the peak areas by fitting Lorentzian functions on the profiles scattered from bccL, bccH and hcp phases for the HPT sample heated up to 1000 K.

of bccH had a fraction of $\sim 60\%$.

3.3. TEM study of the microstructure

Fig. 5a shows a TEM bright-field (BF) image for the microstructure of the HPT-processed HfNbTiZr sample. The average grain size was obtained as ~ 33 nm by averaging the diameters of the grains in many TEM images. **Fig. 5b** shows a HAADF image while the corresponding EDS elemental maps are given in **Fig. 5c-f**. No chemical

inhomogeneities were revealed by these maps. After annealing to 740 K, the grain size was measured as ~ 38 nm which is shown in a typical BF-TEM image in **Fig. 6a** and the nanocrystalline microstructure does not differ significantly from the processed MPEA before heat treatment. The HAADF image in **Fig. 6b** and the elemental maps in **Fig. 6c-f** revealed reasonable chemical homogeneities although XRD showed decomposition into two bcc phases leading to different lattice constants that are most probably caused by different chemical compositions. This apparent contradiction can be explained by the fact that XRD investigates a much larger volume than TEM, therefore the area studied by the latter method may be occasionally free of considerable inhomogeneity.

After heating up to the temperature of 890 K, the grain size determined from the TEM micrographs increased to ~ 81 nm where a representative TEM-BF image of the microstructure is shown in **Fig. 7a**. This value is much larger than that obtained immediately after HPT (~ 33 nm) and after annealing to 740 K (~ 38 nm). The HAADF image in **Fig. 7b** and the corresponding EDS elemental maps in **Fig. 7c-f** indicate considerable chemical inhomogeneities. The element pairs of Zr/Hf and Nb/Ti vary complementary. The highest spatial heterogeneities were observed for Nb and Zr. In practice, the measured chemical composition in some Zr/Hf-rich regions demonstrated the following concentrations (in at.-%): 37–47% Zr, 27–31% Hf, 8–18% Nb and 14–18% Ti, while some Nb/Ti-rich areas showed the following concentrations: 32–36% Nb, 23–24% Ti, 21–25% Zr and 19–20% Hf. It should be noted that grains with different compositions may exist under each other in the TEM sample, therefore the composition measured on a given area may be an average for more than one grain. Nevertheless, it is unambiguously proved that the MPEA material decomposed to Zr/Hf- and Nb/Ti-rich regions which surely correspond to the separate phases bccL and bccH with higher and lower lattice constants, respectively, as observed by XRD in **Fig. 3**, since the atomic sizes of Zr and Hf are much

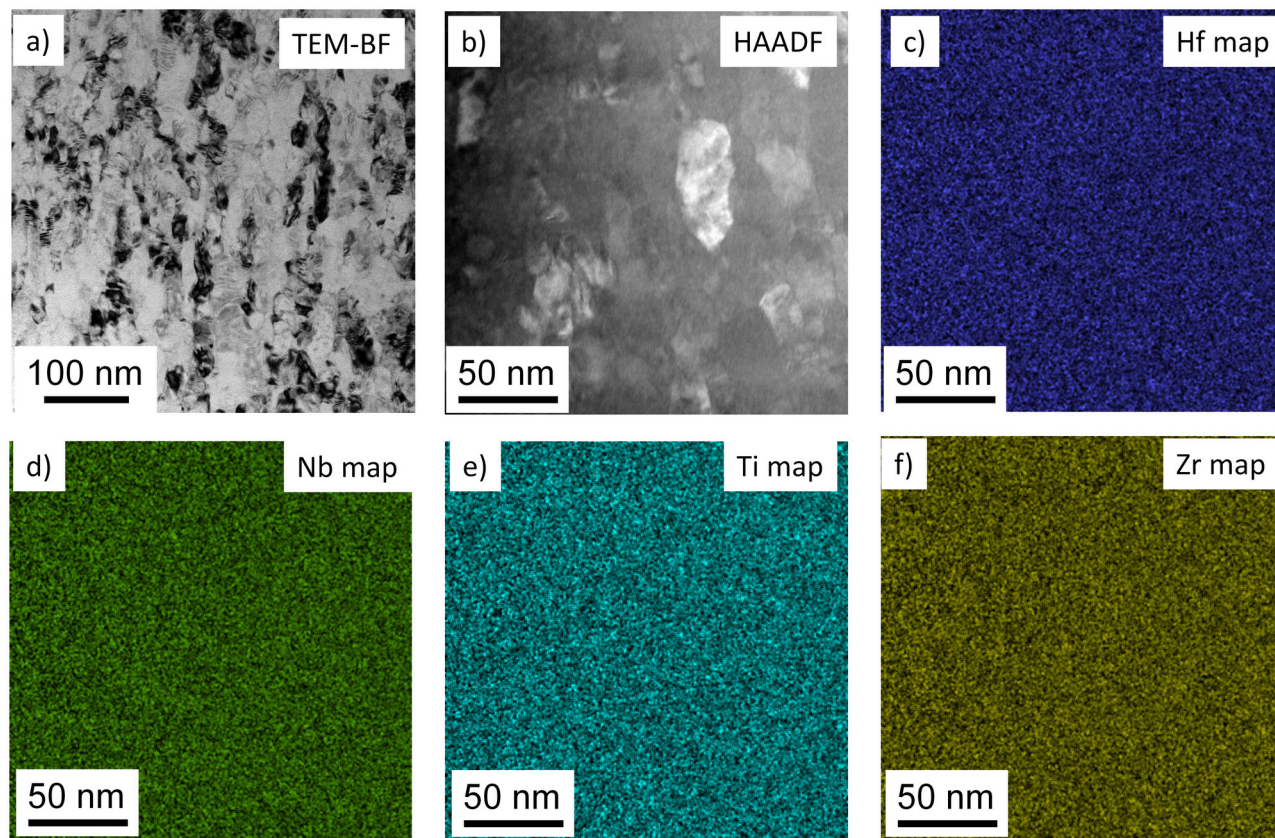


Fig. 5. BF (a) and HAADF (b) images obtained by (S)TEM for the initial HPT-processed sample. The chemical composition for the area shown in (b) was investigated by STEM -EDS. The elemental maps for Hf (c), Nb (d), Ti (e) and Zr (f) are also shown.

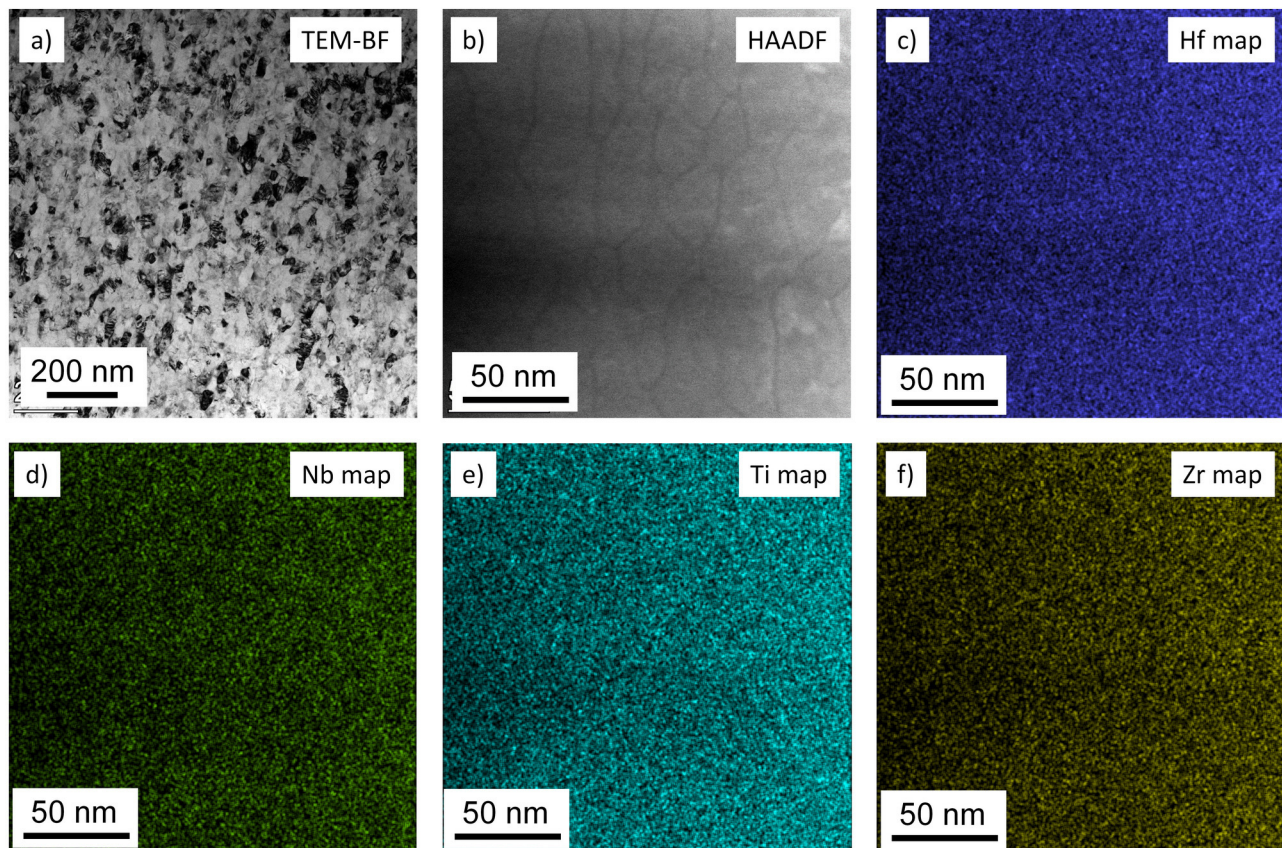


Fig. 6. BF (a) and HAADF (b) images obtained by (S)TEM for the HPT-processed specimen annealed up to 740 K. The chemical composition for the area shown in (b) was investigated by STEM -EDS. The elemental maps for Hf (c), Nb (d), Ti (e) and Zr (f) are also shown.

larger than that for Nb or Ti [24]. XRD also revealed the precipitation of an hcp phase in the annealed MPEA at 890 K (see Section 3.2), but this phase has a very low fraction (~5%) according to XRD and was not observed in the obtained TEM images.

Fig. 8a shows a representative BF-TEM image obtained on the sample heated up to 1000 K. The grain size determined from the TEM images was ~87 nm which only slightly differs from the value obtained for 890 K (~81 nm). A HAADF image and the corresponding EDS maps are presented in Fig. 8b–f. The elemental maps reveal similar chemical inhomogeneities as observed for 890 K, i.e., Zr/Hf- and Nb/Ti-rich regions were identified. After the examination of some Zr/Hf-rich areas, the following concentration ranges were obtained: 41–53% Zr, 27–33% Hf, 1–15% Nb and 12–17% Ti. Similar investigations for the Nb/Ti-rich regions yielded 32–36% Nb, 22–25% Ti, 21–24% Zr and 18–20% Hf. The latter volumes most probably related to the bccH phase identified by XRD since the major element Nb has the lowest atomic radius among the four constituents of the alloy. On the other hand, the Zr/Hf-rich regions correspond ambiguously to the bccL phase. Indeed, a highly magnified HAADF image in Fig. 9a with the corresponding elemental maps in Fig. 9b–e for the alloy annealed to 1000 K reveals that there are Zr/Hf-rich volumes with either bcc or hcp structure. The white cross in Fig. 9b–e indicates a Zr/Hf-rich part where the structure was hcp, while the red cross indicates a Zr/Hf-rich part showing a bcc structure. The corresponding TEM diffraction pattern is shown in Fig. 9f. The measured elemental concentrations were 44% Zr, 29% Hf, 13% Ti and 14% Nb for the bcc phase, and 50% Zr, 36% Hf, 12% Ti and 2% Nb for the hcp phase which was measured on a very thin part of the sample where overlapping of different grains were excluded. This is a reasonable difference between the chemical compositions of the bcc and hcp phases, since among the constituents of this MPEA only Nb has a bcc structure in pure form. Therefore, the higher Nb content could stabilize

the bcc phase while the Nb content below a certain limit formed an hcp structure.

From the TEM-EDS maps, the fraction of the Nb-rich areas was about 70% for both 890 and 1000 K. The Nb-rich regions correspond to phase bccH for which the XRD intensity fraction values were ~54 and ~60% at 890 and 1000 K, respectively. The difference between the XRD and TEM-EDS fractions can be explained by the much smaller volume studied by TEM as compared to XRD. In addition, in the TEM-EDS map we measure the average composition along the beam direction through the local thickness of the TEM lamella. Due to the possible overlap of the grains with different compositions and structures, the separation of the various phases in the map is uncertain.

3.4. Analysis of X-ray line profiles

The breadth and shape of the XRD peak profiles were analyzed for the bcc phase components. Fig. 4 illustrates that as a simple approximation the overlapping peaks were fitted by the sum of Lorentzian functions, therefore the breadth of the peaks for each bcc phase component could be determined. The full width at half maximum (FWHM) of the peaks in the reciprocal space was determined as $FWHM = \cos\theta\Delta(2\theta)/\lambda$ where θ is the Bragg angle, $\Delta(2\theta)$ is the peak breadth in radians and λ is the wavelength of X-rays in nm unit. The FWHM values as a function of the magnitude of the diffraction vector ($g = 2\sin\theta/\lambda$) are plotted in Fig. 10a–c for the bcc components in the HPT-processed specimens followed by annealing at 740 K, 890 K and 1000 K, respectively. This representation of the XRD peak breadths is called as Williamson-Hall plot. For comparison purposes, the peak breadths for the HPT-processed sample are also plotted. It should be noted that this analysis was performed only for six reflections from the seven measured peaks shown in Fig. 2 by eliminating the XRD peak

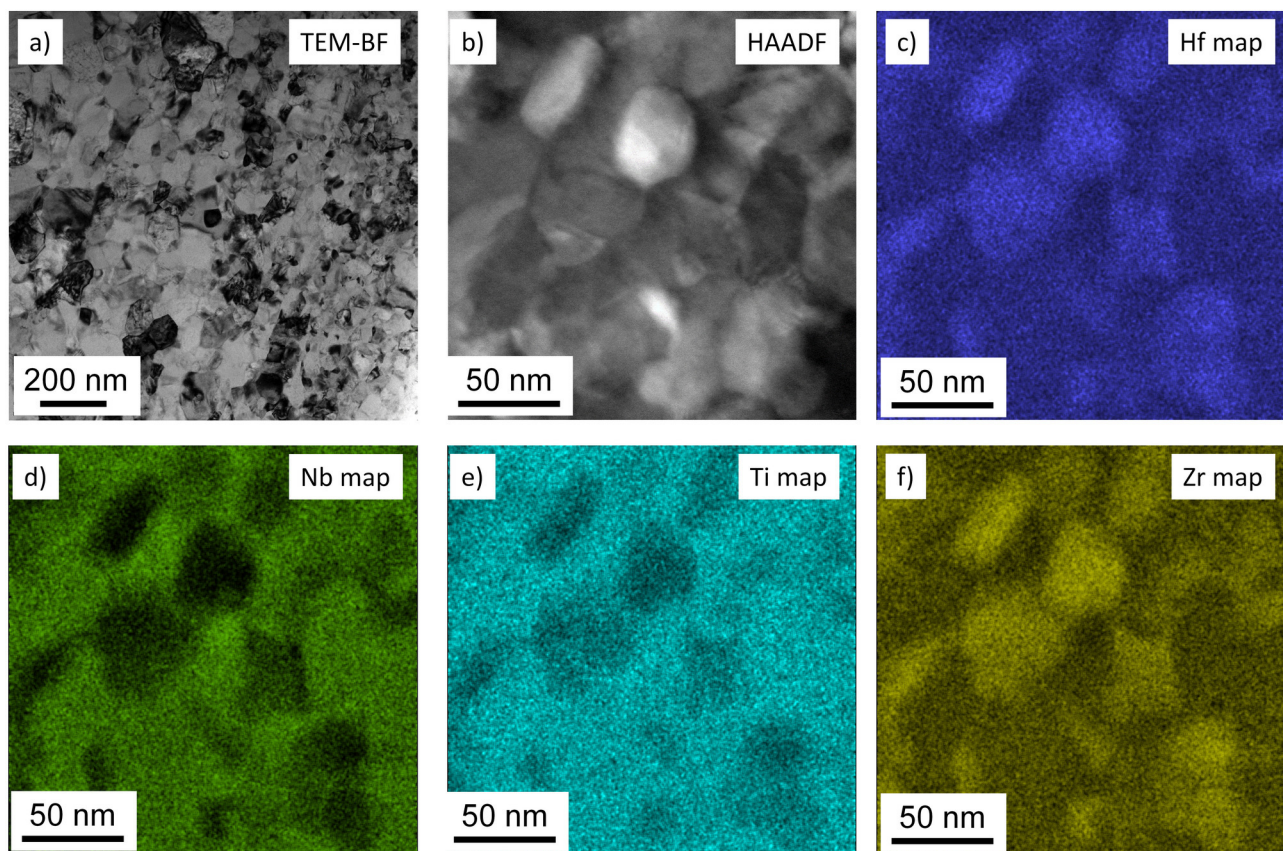


Fig. 7. BF (a) and HAADF (b) images obtained by (S)TEM for the HPT-processed specimen annealed up to 890 K. The chemical composition for the area shown in (b) was investigated by STEM-EDS. The elemental maps for Hf (c), Nb (d), Ti (e) and Zr (f) are also shown.

with the indices 222 that was weak and noisy.

Fig. 10a shows that for the sample heated up to 740 K the peaks of the bccL phase were broader than the HPT-processed sample while the reflections of the bccH phase were narrower than the peaks of the HPT specimen. After heating up to 890 K, the XRD profiles of both bcc components in the annealed sample were narrower than the peaks of the bcc phase in the HPT-processed sample. In addition, the Williamson-Hall plot reveals that the peak breadths are constant for all reflections for the phase bccH suggesting that the peaks were broadened only due to the finite size of the diffraction domains (or crystallites in other words). On the other hand, for the phase bccL the peak breadth increases with increasing the magnitude of the diffraction vector, thereby indicating strain broadening in addition to size broadening. The strain broadening can be caused by lattice defects such as dislocations developed during HPT-processing and/or by chemical heterogeneities in the studied phase [25–27]. Thus, it can be concluded that in the phase bccH at 890 K the remaining dislocation density is negligible and there is no considerable chemical inhomogeneity. After heating up to 1000 K as seen in Fig. 10c, the phase bccH exhibits strain broadening beside size broadening while for phase bccL only size broadening was observed.

The dislocation density and the diffraction domain size were evaluated quantitatively from the XRD peak profiles using the CMWP fitting procedure. In this method, the theoretical peak profile is calculated for each reflection assuming that the peak broadening is caused by the finite crystallite size and dislocations. Fig. 11 illustrates CMWP fitting of a part of the XRD pattern for the HPT-processed HfNbTiZr MPEA specimen. In order for a better visibility of the agreement between the measured and fitted patterns, only a part of the fitted diffractogram is shown in this figure, but the fitting was carried out in the whole measured diffraction angle range (between 30 and 120°). For the heat

treated samples, the bcc phase was assumed to have two components (bccL and bccH), therefore each measured bcc profile was fitted with two overlapping theoretical functions which depend on the crystallite sizes and the dislocation densities of the two bcc phase components. The peaks of the hcp phase were not fitted due to their relatively low intensity; rather they were put into the background. The average diffraction domain sizes and the average dislocation densities obtained by the CMWP method are listed in Table 2. In the initial single-phase HPT-processed sample, the diffraction domain size was ~ 15 nm and the dislocation density was $\sim 219 \times 10^{14} \text{ m}^{-2}$. The grain size determined by TEM is slightly larger than the domain size obtained by XLPA. This difference may be caused by the much better statistics of the XLPA method compared to TEM since the former procedure studies orders of magnitude larger volume [27].

In the sample heated up to 740 K, the diffraction domain size of the major bccH phase is ~ 24 nm and the dislocation density is $\sim 36 \times 10^{14} \text{ m}^{-2}$ which are higher and lower, respectively, than the values obtained for the HPT specimen. In the meantime, the dislocation density in the bccL phase was similar or only slightly higher than that for the HPT-processed specimen. After annealing up to 890 K, the domain size in the major bccH phase was ~ 47 nm and the dislocation density decreased below the lower detection limit for the present XLPA ($\sim 10^{13} \text{ m}^{-2}$). This very low dislocation density is in agreement with the lack of strain broadening in the Williamson-Hall plot for this phase (see Fig. 10b). On the other hand, for the phase bccL a relatively large dislocation density of $\sim 164 \times 10^{14} \text{ m}^{-2}$ was detected. In the specimen heated up to 1000 K, the major bccH phase has a domain size of ~ 12 nm and a dislocation density of $\sim 92 \times 10^{14} \text{ m}^{-2}$ while negligible dislocation density was detected for the phase bccL in accordance with the lack of strain broadening in the Williamson-Hall plot (see Fig. 10c). For this phase, the crystallite size was about 52 nm. It should be noted

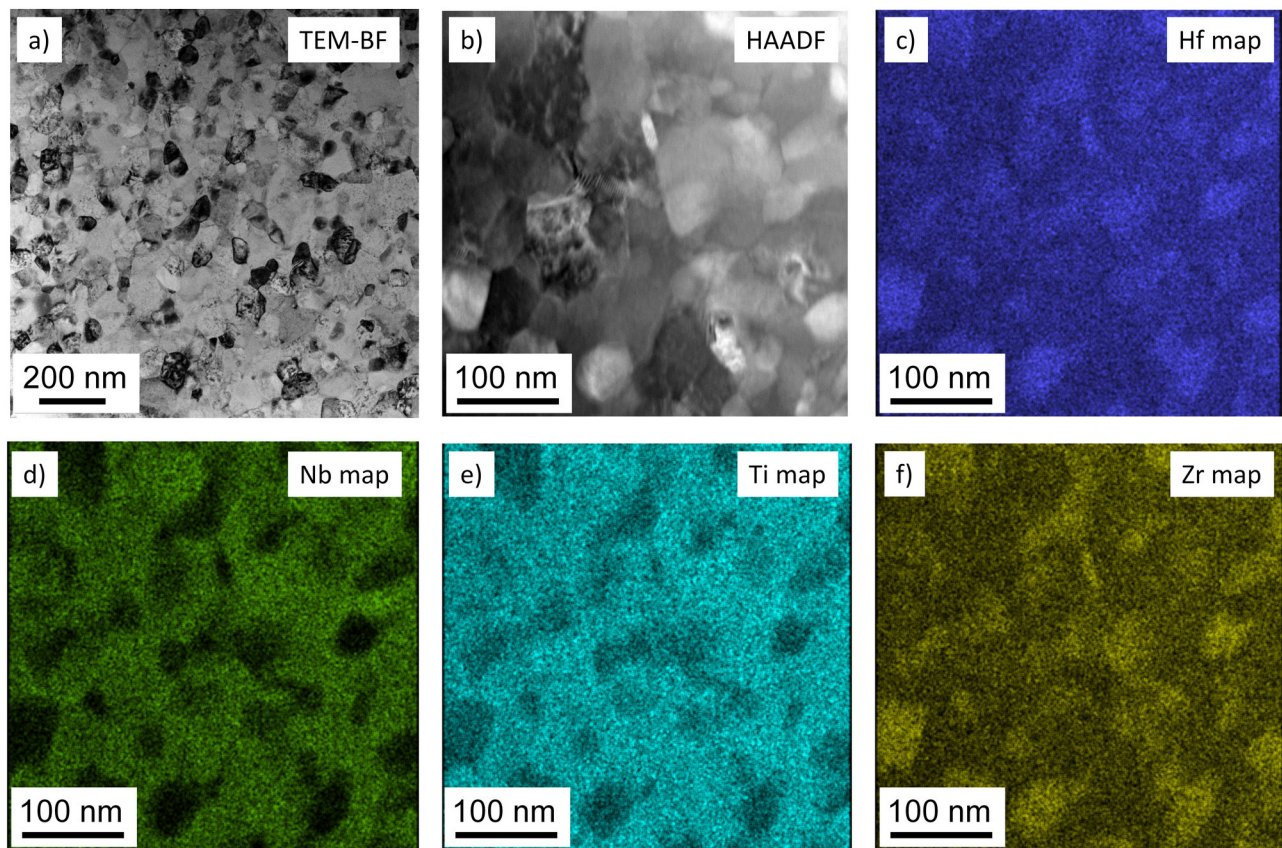


Fig. 8. BF (a) and HAADF (b) images obtained by (S)TEM for the HPT-processed specimen annealed up to 1000 K. The chemical composition for the area shown in (b) was investigated by STEM -EDS. The elemental maps for Hf (c), Nb (d), Ti (e) and Zr (f) are also shown.

that for the annealed samples the real dislocation densities may be somewhat lower than the values obtained by XLPA due to the inevitable counting of chemical inhomogeneities in the bcc phases that may contribute to strain broadening in addition to dislocations.

3.5. Change of the hardness during annealing

Fig. 12 shows the evolution of the microhardness as a function of the temperature of annealing for the HPT-processed HfNbTiZr MPEA. The hardness of the HPT sample was 4420 ± 200 MPa and it remained practically unchanged after annealing up to 740 K. In this state, the hardness was measured as 4610 ± 350 MPa. Thereafter, heating of the HPT sample up to 890 K resulted in softening to 3620 ± 340 MPa. With increasing the temperature to 1000 K, the hardness further decreased to 3100 ± 300 MPa.

4. Discussion

4.1. Evolution of the phase composition during annealing

The decomposition of different MPEAs during annealing has been studied both experimentally [19,24,28,29] and theoretically using thermodynamic simulations [19]. To the knowledge of the authors, such an investigation has not been performed for the four-component HfNbTiZr MPEA. In the meantime, the thermal stability of the five-component HfNbTaTiZr HEA has been extensively studied [19,24]. That material contained an additional fifth component of Ta besides all the four constituents of the presently studied MPEA. Numerical simulations with Calphad software revealed the equilibrium phase composition of the five-component HfNbTaTiZr MPEA in a temperature range between 0 and 2500 °C [19].

Based on the reported data, Fig. 13 shows the variation of the fractions of the equilibrium phases in HfNbTaTiZr alloy as a function of temperature in a range between 400 and 1100 K that is interesting to our research. The dashed vertical lines indicate the temperatures at which our HfNbTiZr MPEA was investigated. It can be seen that at 740 K an Nb/Ta-rich bcc phase and a Zr/Hf/Ti-rich hcp phase coexist with fractions of 45% and 55%, respectively. Contrary to this prediction, the present nanocrystalline HfNbTiZr MPEA heat treated up to 740 K contained two bcc phases with different lattice constants. The phase bccH is the main phase with a fraction of 71% while bccL has a higher lattice constant and a fraction of 29% (see Table 1). Considering the atomic radii of the constituent elements of HfNbTiZr, the phase bccL was most probably enriched in Zr and/or Hf while the phase bccH was enriched in Nb and/or Ti. The existence of a Nb-rich bcc phase is in accordance with the result of the Calphad calculation performed for HfNbTaTiZr (see Fig. 13) but instead of the Zr/Hf-rich hcp phase a bcc phase was detected in our material. The nucleation of the hcp phase in the bcc HfNbTaTiZr and HfNbTiZr alloys may start with a spinodal decomposition, similar to the process observed in HfNbTaZr [30]. Thus, when decomposition starts in the bcc HfNbTiZr alloy most probably the Zr/Hf-rich regions form first with maintaining the bcc crystal structure. If the heat treatment was long enough, the bcc structure in the Zr/Hf-rich volumes would transform into an hcp structure. Therefore, the bccL phase can be considered as an intermediate metastable phase during the formation of a Zr/Hf-rich hcp structure.

Fig. 3 and Table 1 reveal that at 890 K an hcp phase formed but its fraction is very low (about 5%) and the main phases are the two bcc structures with slightly different lattice constants. EDS elemental maps in Fig. 7 suggest that the two bcc phases with lower and higher lattice parameters are Nb- and Zr/Hf-rich phases, respectively. Considering the equilibrium phase composition calculated for HfNbTaTiZr (see Fig. 13),

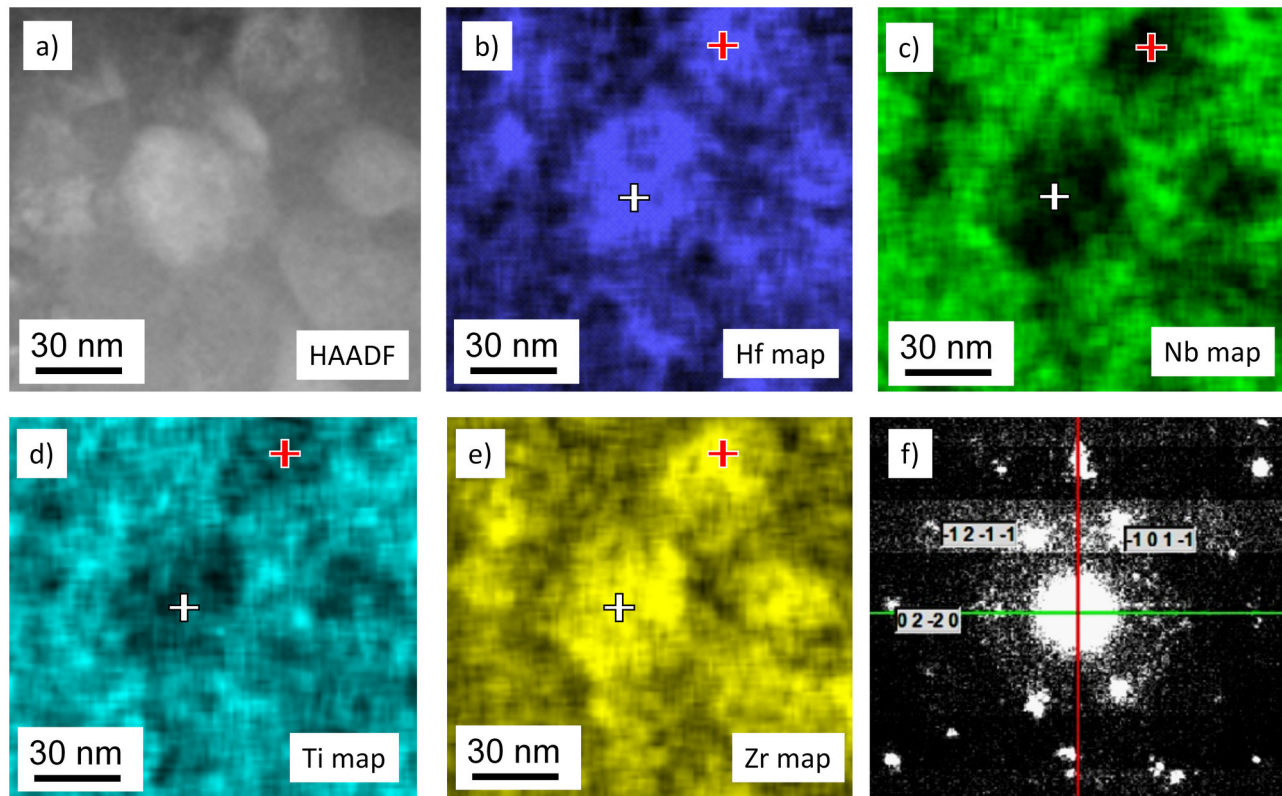


Fig. 9. A HAADF image (a) and the corresponding elemental maps for Hf (b), Nb (c), Ti (d) and Zr (e) in the case of the sample annealed up to 1000 K after HPT. The white cross indicates a Zr/Hf-rich part where the structure was hcp. The corresponding TEM diffraction pattern is shown in (f). The red cross indicates a Zr/Hf-rich part where the structure was bcc. (For interpretation of the references to colour in this figure legend, the reader is referred to the web version of this article.)

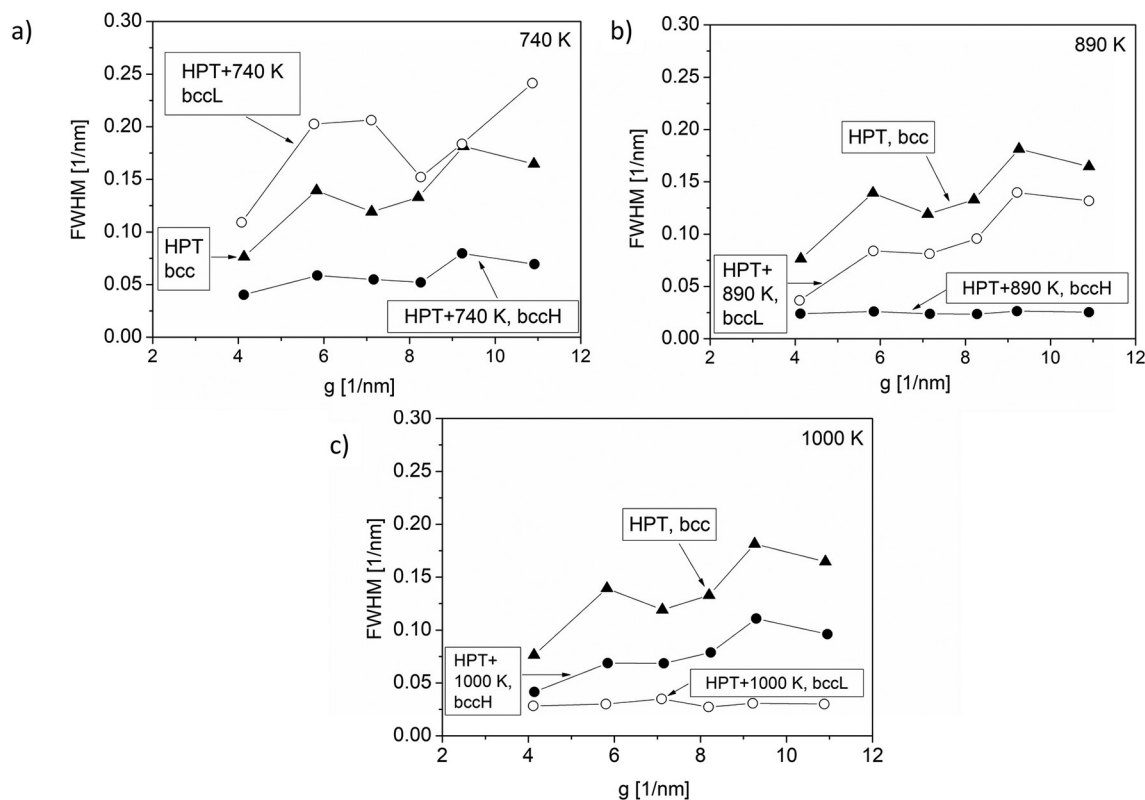


Fig. 10. Williamson-Hall plots of the full width at half maximum (FWHM) versus the magnitude of the diffraction vector (g) for the separated profiles of the different phases after annealing at 740 K (a), 890 K (b) and 1000 K (c).

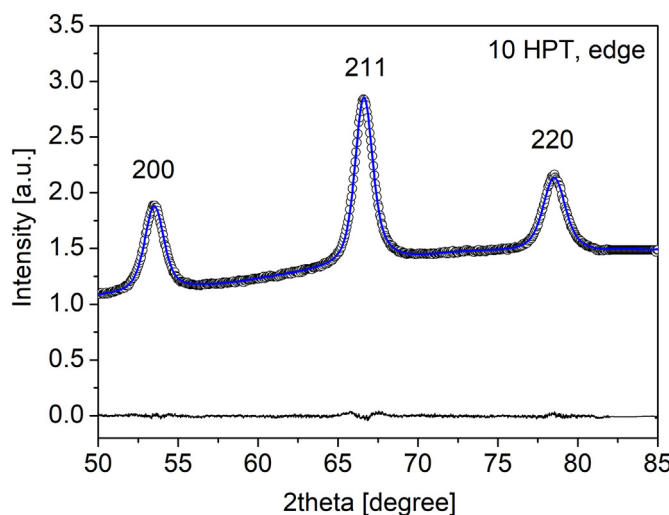


Fig. 11. CMWP fitting showing only for a part of the diffractogram taken on the HPT-processed sample. The black open circles and the blue solid line show the measured and the fitted patterns, respectively. The difference between them is shown at the bottom of the figure. (For interpretation of the references to colour in this figure legend, the reader is referred to the web version of this article.)

Table 2

The diffraction domain size and the dislocation density determined by XLPA for the bcc phases, as well as the grain size obtained by TEM. BccL and bccH indicate the bcc phases for which the XRD peaks appeared at lower and higher diffraction angles, respectively (see Fig. 3).

State of material	Phases	Diffraction domain size [nm]	Dislocation density $[10^{14} \text{ m}^{-2}]$	Grain size [nm]
10 HPT	bcc	15 ± 2	219 ± 24	33
10 HPT + 740 K	bccL	24 ± 4	265 ± 45	38
	bccH	24 ± 3	36 ± 5	
10 HPT + 890 K	bccL	21 ± 3	164 ± 18	81
	bccH	47 ± 6	< 0.1	
10 HPT + 1000 K	bccL	52 ± 6	< 0.1	87
	bccH	12 ± 2	92 ± 10	

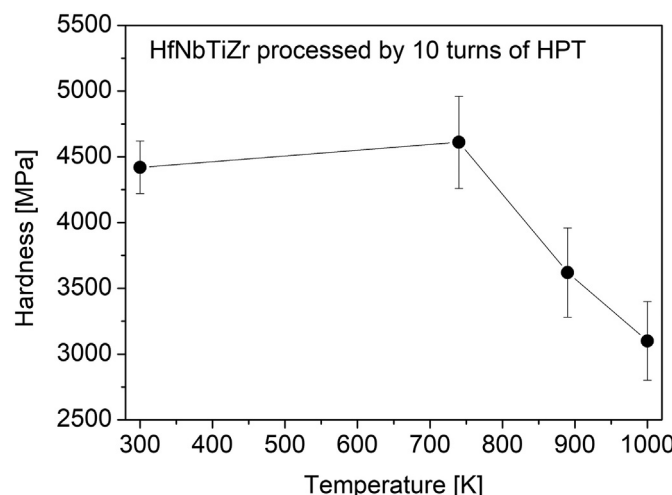


Fig. 12. The hardness versus the annealing temperature.

the HPT-processed HfNbTiZr sample annealed up to 890 K is yet far from equilibrium since a higher hcp phase content would be expected. Nevertheless, the lattice constants of the bccL phase decreased compared to 740 K due to the precipitation of the hcp structure from this phase since the hcp phase is richer in Zr and Hf. The lattice constant of

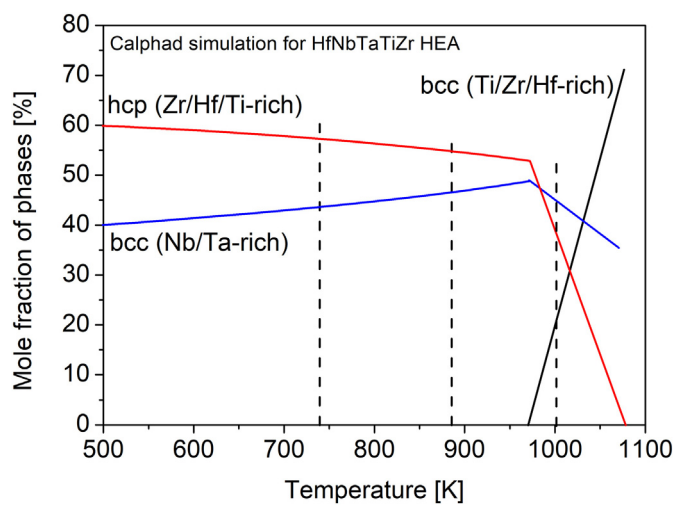


Fig. 13. The variation of the fractions of the different phases for HfNbTaTiZr MPEA as a function of the temperature as calculated from former Calphad modeling [13].

the bccH phase in HfNbTiZr increased when the temperature changed from 740 to 890 K. Calphad calculation for HfNbTaTiZr also revealed similar trend which was caused by the decrease of the Nb content in this phase with increasing temperature (see Fig. 8d in [19]).

At 1000 K, the Calphad simulation for the HfNbTaTiZr alloy suggests the co-existence of three phases: a Nb/Ta-rich bcc phase with the fraction of $\sim 45\%$, another bcc phase enriched in Ti, Zr and Hf (fraction: $\sim 20\%$) and a Zr/Hf/Ti-rich hcp phase with the fraction of $\sim 35\%$. Our sample also contained two bcc phases and one hcp structure, although their experimentally determined fractions differ from the values calculated for HfNbTaTiZr. Both the bccL phase with higher lattice constant and the hcp phase surely correspond to the Zr/Hf-rich regions in the present four-element MPEA heated up to 1000 K. The EDS analysis at the bcc and hcp areas in Fig. 9 suggested that the hcp phase is more depleted from Nb than the bcc phase (see the compositions in Section 3.3). This conclusion is reasonable since Nb is the only element in the four constituents having a bcc structure in a pure form while the others have an hcp structure. Thus, Nb tends to stabilize a bcc structure in the HfNbTiZr MPEA and when the Nb content decreases under a limit, the alloy transforms into an hcp structure. It should be emphasized that the bccL phase at 890 K differs from the bccL phase at 1000 K. At 1000 K, the bccL phase is a newly nucleated Zr/Hf-rich structure as suggested by Calphad simulations for HfNbTaTiZr [19]. All other bcc volumes are in the bccH phase. The center of the broad peak of bccH phase is at a relatively high angle at 1000 K due to the enrichment of this phase with Nb since both the hcp and the Zr/Hf-rich bcc phases contain low amount of Nb.

The differences between the phase composition measured on the HfNbTaTiZr and HfNbTiZr alloys at 1000 K can be explained by (i) the apparently different chemical compositions of the two alloys, (ii) the present DSC annealing was short so that there was not enough time to achieve the equilibrium at 1000 K and (iii) the XRD intensity fractions listed in Table 1 may differ from the mole fractions of the phases. Nevertheless, the higher the temperature of the DSC annealing for the HPT-processed HfNbTiZr MPEA, the closer its phase composition to the simulated results obtained for HfNbTaTiZr. For a more reliable theoretical assessment of the evolution of the phase composition in the HfNbTiZr MPEA, simulations for this composition are necessary which is out of the scope of this study.

4.2. Effect of heat treatment on microstructure

The changes in the XRD peak profiles revealed the evolution of the

microstructure after heating up to different temperatures. At 740 K, the HPT-processed microstructure was recovered partially, namely in phase bccH, the dislocation density decreased from $\sim 219 \times 10^{14} \text{ m}^{-2}$ to $\sim 36 \times 10^{14} \text{ m}^{-2}$ while the grain and diffraction domain sizes increased slightly (see Table 2). At the same time, the dislocation density in phase bccL did not decrease. As the lattice constant of this phase was higher than for the HPT-processed sample, the bccL phase was surely enriched with large atoms such as Zr and Hf. Larger atoms pin dislocations more effectively, which may cause a less pronounced or negligible recovery in the phase bccL. Considering the phase fractions and the dislocation densities listed in Tables 1 and 2, respectively, the average dislocation density decreased from $\sim 219 \times 10^{14} \text{ m}^{-2}$ to $\sim 102 \times 10^{14} \text{ m}^{-2}$ during heating up to 740 K. It should be noted, however, that the peaks of the phase bccL were relatively weak (see Fig. 3), therefore the parameters of the microstructure determined from these peaks have a higher uncertainty. It is also noted that although the peak breadths for the phase bccL at 740 K are higher than that for the HPT-processed sample in the Williamson-Hall plot shown in Fig. 10a, this is not in a contradiction with the similar microstructural parameters of the bccL phase and the HPT specimen (see Table 2). This apparent dichotomy was caused by the fact that for the Williamson-Hall plots the peak breadths were determined by the decomposition of the overlapping XRD peaks using Lorentzian functions while in the CMWP analysis the peak profile functions were calculated directly from the microstructure and these functions usually have no Lorentzian shape. Nevertheless, the Lorentzian decomposition of XRD profiles is a suitable method for revealing the difference in the peak breadth evolutions for the bccL and bccH phases.

After heating up to 890 K, the dislocation density further decreased in both the bccL and bccH phases and the diffraction domain size increased to about 47 nm in the bccH phase (see Table 2). In addition, the grain size determined by TEM increased from ~ 38 to ~ 81 nm when the temperature increased from 740 to 890 K (see Fig. 14), which suggests that grain coarsening occurred in addition to recovery in this temperature range. Using the fractions and the dislocation densities of the two bcc phases, an average dislocation density of $\sim 67 \times 10^{14} \text{ m}^{-2}$ was calculated for the sample annealed to 890 K. It should be noted that the chemical inhomogeneities can also cause strain-like broadening of the XRD profiles. Namely, the chemical heterogeneities can yield a spatial variation of the lattice spacing in the material, thereby resulting in an XRD peak broadening which resembles the broadening caused by microstrains [25–27]. Therefore, the dislocation density values determined by XLPA and listed in Table 2 for 890 K may overestimate the real values, i.e., the average dislocation density may be lower than $\sim 67 \times 10^{14} \text{ m}^{-2}$.

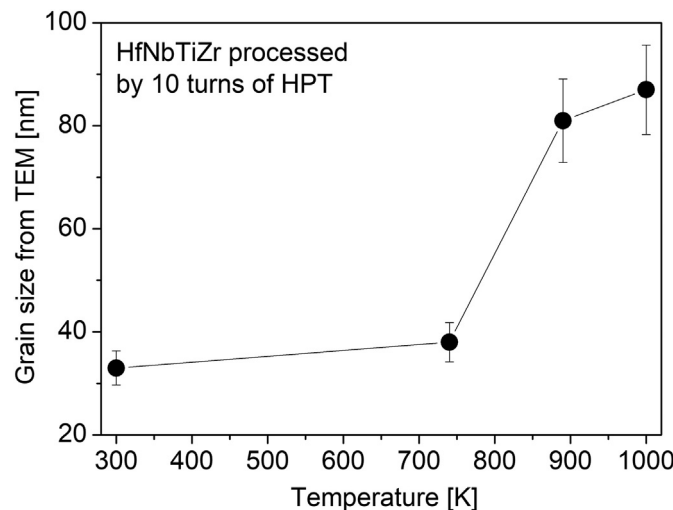


Fig. 14. The grain size determined by TEM versus the annealing temperature.

After heating the HPT-processed MPEA up to 1000 K, chemical inhomogeneities were observed (see Section 3.3), therefore the measured dislocation density of $\sim 92 \times 10^{14} \text{ m}^{-2}$ for the phase bccH may be larger than the real value. Even if this situation occurs, the average dislocation density cannot be higher than $\sim 55 \times 10^{14} \text{ m}^{-2}$, i.e., the recovery of the microstructure certainly continued between 890 and 1000 K. In this averaging, the bccL phase with narrow XRD peaks was also taken into account. This phase is practically defect-free according to the Williamson-Hall analysis of the XRD profiles (see Fig. 10), i.e., the peaks were broadened only due to the small diffraction domain size. The bccL phase at 1000 K is a Zr/Hf-rich bcc structure which most probably was newly nucleated between 890 and 1000 K as suggested by the phase fraction evolution calculated for the HfNbTaTiZr MPEA using Calphad software (see Fig. 13). As noted earlier in the TEM-EDS experiments, there is a large scattering in the Nb concentration of the Zr/Hf-rich part of the sample heated up to 1000 K. Fig. 9 suggests that the regions with a few percentages of Nb were transformed into a hcp structure. As this hcp phase has a relatively low intensity fraction (about 12%), its peak profiles were not evaluated for the microstructure by the CMWP software. However, the peak breadth analysis indicates that the diffraction domain size of the hcp phase was about 30–40 nm.

On the basis of the results obtained for the variation of the phase composition and the microstructure during annealing, the processes occurring during the heat treatments in the different temperature regions are summarized in Table 3 by considering these processes as the sources of the exothermic heats evolved in the DSC thermogram as shown in Fig. 1. Up to 740 K, the decomposition into two bcc phases and the recovery in the bccH phase contributed to the heat released during annealing. Beside dislocations, the annihilation of other defects, such as vacancies, may also have a contribution to the exotherm peak evolved between 400 and 740 K as reported earlier that a very high excess vacancy concentration in the order of magnitude of 10^{-4} can form during SPD-processing [31–33]. Between 740 and 890 K, recovery in both bcc phases, grain growth and nucleation of a new hcp phase yielded the heat evolution. Finally, between 890 and 1000 K further recovery, increase of the hcp phase fraction and nucleation of a new Zr/Hf-rich bcc phase occurred and these processes contributed to the heat released during the DSC experiment.

4.3. Influence of the microstructure changes on the hardness

The hardness variation due to heating up to 740, 890 and 1000 K was revealed in Fig. 12. The microhardness of the HPT-processed HfNbTiZr MPEA remained unchanged after annealing up to 740 K even if the average dislocation density decreased from $\sim 219 \times 10^{14} \text{ m}^{-2}$ to $\sim 102 \times 10^{14} \text{ m}^{-2}$. The softening effect of this recovery may be compensated by the annealing-induced hardening phenomena [34–37]. It has been shown that annealing of nanocrystalline alloys can result in hardening due to the annihilation of mobile dislocations and the relaxation of grain boundaries. The relaxed grain boundaries can emit dislocations harder than the boundaries in the SPD-processed materials, thereby resulting in hardening. This effect usually occurs only at moderate temperatures ($0.3\text{--}0.4 \times T_m$, where T_m is the melting point) and this temperature range corresponds to 620–820 K for the HfNbTiZr MPEA. Therefore, the anneal-hardening can compensate the softening caused by recovery and yielding an unchanged hardness at 740 K. Between 740 and 890 K there is a significant softening that may be caused by the considerable increase of the grain size and the further reduction of the dislocation density. Between 890 and 1000 K, further grain coarsening was not observed but the average dislocation density slightly decreased. This effect can explain the slight softening between 890 and 1000 K.

5. Summary and conclusions

The thermal stability of the nanostructure formed during HPT-

Table 3

The processes occurring in the different temperature ranges of annealing by DSC at a rate of 40 K/min.

300–740 K	740–890 K	890–1000 K
1. Decomposition into two bcc phases	1. Grain coarsening	1. Recovery
2. Recovery in phase bccH	2. Recovery in both bcc phases	2. Increase of the hcp phase fraction
	3. Nucleation of a hcp phase	3. Nucleation of a defect-free bccL phase

processing of an HfNbTiZr MPEA was investigated. First, a DSC thermogram was taken which contained three strongly overlapping exothermic peaks. Then, samples were heated up to the characteristic temperatures of the DSC curve and the evolution of the microstructure and the phase composition were analyzed. The following conclusions were drawn from the results:

1. During annealing up to a temperature of 740 K, the single-phase bcc MPEA decomposed into two bcc structures with lower (~ 0.3427 nm) and higher (~ 0.3485 nm) lattice constants as compared to the initial state (~ 0.3438 nm). The major bcc phase with the lower lattice parameter exhibited a recovery where the dislocation density considerably decreased from $\sim 219 \times 10^{14}$ m $^{-2}$ to $\sim 36 \times 10^{14}$ m $^{-2}$ while the grain size remained consistent (~ 20 nm). The hardness remained unchanged (~ 4500 MPa) after annealing up to 740 K. Most probably, the softening caused by recovery was compensated by the hardening induced by grain boundary relaxation and annihilation of mobile dislocations, resulting in an unchanged hardness.
2. The heat treatment between 740 and 890 K resulted in the nucleation of a Zr/Hf-rich hcp phase with a low XRD intensity fraction of about 5%. At 890 K, the major bcc phase had two components with slightly different lattice constants. These two components are Zr/Hf-rich and Nb-rich bcc structures with higher and lower lattice parameters, respectively. Due to recovery, lowering of dislocation density towards $< 10^{13}$ m $^{-2}$ was more pronounced in the Nb-rich phase, while the grain size significantly increased to ~ 81 nm. The hardness decreased from ~ 4500 to ~ 3600 MPa due to these changes in the microstructure.
3. Annealing up to 1000 K led to an increase of the XRD intensity fraction of the Zr/Hf-rich hcp phase to $\sim 12\%$. In addition, a defect-free Zr/Hf-rich bcc phase was formed. The increase of the grain size between 890 and 1000 K was marginal (from ~ 81 to ~ 87 nm) while a decrease of the dislocation density was also detected. These microstructural changes yielded only a slight decrease of the hardness from ~ 3600 to ~ 3100 MPa between 890 and 1000 K.

Declaration of competing interest

The authors declare that they have no known competing financial interests or personal relationships that could have appeared to influence the work reported in this paper.

Acknowledgement

This work was supported in part by the Ministry of Human Capacities of Hungary within the ELTE University Excellence program (1783-3/2018/FEKUTSRAT); in part by the grant no. VEKOP-2.3.3-15-2016-00002 of the European Structural and Investment Funds; and in part by the National Science Foundation of the United States under Grant No. DMR-1810343. The preparation of the TEM lamellae by Levente Illés is also acknowledged.

Data availability

The raw/processed data required to reproduce these findings cannot be shared at this time due to technical or time limitations.

References

- [1] B. Cantor, I.T.H. Chang, P. Knight, A.J.B. Vincent, Microstructural development in equiatomic multicomponent alloys, *Mater. Sci. Eng. A* 375 (2004) 213–218.
- [2] J.W. Yeh, S.K. Chen, S.J. Lin, J.Y. Gan, T.S. Chin, T.T. Shun, C.H. Tsau, S.Y. Chang, Nanostructured high-entropy alloys with multiple principal elements: novel alloy design concepts and outcomes, *Adv. Eng. Mater.* 6 (2004) 299–303.
- [3] Y. Ikeda, B. Grabowski, F. Körmann, Ab initio phase stabilities and mechanical properties of multicomponent alloys: a comprehensive review for high entropy alloys and compositionally complex alloys, *Mater. Charact.* 147 (2019) 464–511.
- [4] B. Gludovatz, A. Hohenwarter, D. Catoor, Edwin H. Chang, E. P. George, R. O. Ritchie, A fracture-resistant high-entropy alloy for cryogenic applications, *Science* 345 (2014) 1153–1158.
- [5] M.H. Chuang, M.H. Tsai, W.R. Wang, S.J. Lin, J.W. Yeh, Microstructure and wear behavior of Al_{0.5}Cr_{0.5}FeNi_{1.5}Ti_{0.5} high-entropy alloys, *Acta Mater.* 59 (2011) 6308–6317.
- [6] P. Kozelj, S. Vrtnik, A. Jelen, S. Jazbec, Z. Jaglicic, S. Maiti, M. Feuerbacher, W. Steurer, J. Dolinsek, Discovery of a superconducting high-entropy alloy, *Phys. Rev. Lett.* 113 (2014) 107001.
- [7] O.N. Senkov, D.B. Miracle, K.J. Chaput, J.P. Couzinie, Development and exploration of refractory high entropy alloys—a review, *J. Mater. Res.* 33 (2018) 3092–3128.
- [8] Y.D. Wu, Y.H. Cai, T. Wang, J.J. Si, J. Zhu, Y.D. Wang, X.D. Hui, A refractory Hf₂₅Nb₂₅Ti₂₅Zr₂₅ high-entropy alloy with excellent structural stability and tensile properties, *Mater. Lett.* 130 (2014) 277–280.
- [9] J. Gubicza, A. Heczel, M. Kawasaki, J.K. Han, Y. Zhao, Y. Xue, S. Huang, J.L. Lábár, Evolution of microstructure and hardness in Hf₂₅Nb₂₅Ti₂₅Zr₂₅ high-entropy alloy during high-pressure torsion, *J. Alloys Compd.* 788 (2019) 318–328.
- [10] M.J. Haché, C. Cheng, Y. Zou, Nanostructured high-entropy materials, *J. Mater. Res.* 35 (2020) 1051–1075.
- [11] F. Otto, A. Dlouhý, K.G. Pradeep, M. Kuběnová, D. Raabe, G. Eggeler, E.P. George, Decomposition of the single-phase high-entropy alloy CrMnFeCoNi after prolonged anneals at intermediate temperatures, *Acta Mater.* 112 (2016) 40–52.
- [12] B. Schuh, B. Völker, V. Maier-Kiener, J. Todt, J. Li, A. Hohenwarter, Phase decomposition of a single-phase AlTiVNb high-entropy alloy after severe plastic deformation and annealing, *Adv. Eng. Mater.* 19 (2017) 1600674.
- [13] M.E. Bloomfield, K.A. Christofidou, N.G. Jones, Effect of Co on the phase stability of CrMnFeCoNi high entropy alloys following long-duration exposures at intermediate temperatures, *Intermetallics* 114 (2019) 106582.
- [14] K.A. Christofidou, E.J. Pickering, P. Orsatti, P.M. Mignanelli, T.J.A. Slater, H.J. Stone, N.G. Jones, On the influence of Mn on the phase stability of the CrMnFeCoNi high entropy alloys, *Intermetallics* 92 (2018) 84–92.
- [15] K.A. Christofidou, T.P. McAuliffe, P.M. Mignanelli, H.J. Stone, N.G. Jones, On the prediction and the formation of the sigma phase in CrMnCoFeNi high entropy alloys, *Journal of Alloys and Compounds* 770 (2019) 285–293.
- [16] N.Y. Yurchenko, N.D. Stepanov, M.A. Tikhonovsky, G.A. Salishchev, Phase evolution of the Al_xNbTiV_z (x=0; 0.5; 1; 1.5) high entropy alloys, *Metals* 6, no. 12 (2016) 298.
- [17] N.Y. Yurchenko, N.D. Stepanov, A.O. Gridneva, M.V. Mishunin, G.A. Salishchev, S.V. Zherebtsov, Effect of Cr and Zr on phase stability of refractory Al–Cr–Nb–Ti–V–Zr high-entropy alloys, *J. Alloys Compd.* 757 (2018) 403–414.
- [18] B. Schuh, F. Mendez-Martin, B. Völker, E.P. George, H. Clemens, R. Pippan, A. Hohenwarter, Mechanical properties, microstructure and thermal stability of a nanocrystalline CoCrFeMnNi high-entropy alloy after severe plastic deformation, *Acta Mater.* 96 (2015) 258–268.
- [19] B. Schuh, B. Völker, J. Todt, N. Schell, L. Perrière, J. Li, J.P. Couzinié, A. Hohenwarter, Thermodynamic instability of a nanocrystalline, single-phase Ti₂Zr₂Nb₂Hf₂Ta₂ alloy and its impact on the mechanical properties, *Acta Mater.* 142 (2018) 201–212.
- [20] N.D. Stepanov, N.Y. Yurchenko, S.V. Zherebtsov, M.A. Tikhonovsky, G.A. Salishchev, Aging behavior of the HfNbTaTiZr high entropy alloy, *Mater. Lett.* 211 (2018) 87–90.
- [21] R.B. Figueiredo, P.R. Cetlin, T.G. Langdon, Using finite element modeling to examine the flow processes in quasi-constrained high-pressure torsion, *Mater. Sci. Eng. A* 528 (2011) 8198–8204.
- [22] J.B. Nelson, D.P. Riley, An experimental investigation of extrapolation methods in the derivation of accurate unit-cell dimensions of crystals, *Proc. Phys. Soc.* 57 (1945) 160–177.
- [23] G. Ribárik, J. Gubicza, T. Ungár, Correlation between strength and microstructure of ball-milled Al–Mg alloys determined by X-ray diffraction, *Mater. Sci. Eng. A* 387 (2004) 343–347.
- [24] J.Q. Yao, X.W. Liu, N. Gao, Q.H. Jiang, N. Li, G. Liu, W.B. Zhang, Z.T. Fan, Phase stability of a ductile single-phase BCC Hf_{0.5}Nb_{0.5}Ta_{0.5}Ti_{1.5}Zr refractory high-entropy alloy, *Intermetallics* 98 (2018) 79–88.
- [25] A. Leineweber, E.J. Mittemeijer, Diffraction line broadening due to lattice-

parameter variations caused by a spatially varying scalar variable: its orientation dependence caused by locally varying nitrogen content in ϵ -FeN_{0.433}, *J. Appl. Crystallogr.* 37 (2004) 123–135.

[26] A. Leineweber, E.J. Mittemeijer, Anisotropic microstrain broadening due to compositional inhomogeneities and its parametrisation, *Z. Krist. (Supplement 23)* (2006) 117–122.

[27] J. Gubicza, X-ray Line Profile Analysis in Materials Science, IGI-Global, Hershey, USA, 2014.

[28] D. Kumar, O. Maulik, S. Kumar, Y.V.S.S. Prasad, V. Kumar, Phase and thermal study of equiatomic AlCuCrFeMnW high entropy alloy processed via spark plasma sintering, *Mater. Chem. Phys.* 210 (2018) 71–77.

[29] V. Chaudhary, B. Gwalani, V. Soni, R.V. Ramanujan, R. Banerjee, Influence of Cr Substitution and Temperature on Hierarchical Phase Decomposition in the AlCoFeNi High Entropy Alloy, *Scientific Reports* 8 (2018) 15578.

[30] T.Y. Liu, J.C. Huang, W.S. Chuang, H.S. Chou, J.Y. Wei, C.Y. Chao, Y.C. Liao, J.S.C. Jang, Spinodal decomposition and mechanical response of a TiZrNbTa high-entropy alloy, *Materials* 12 (2019) 3508.

[31] E. Schäfer, G. Steiner, E. Korznikova, M. Kerber, M.J. Zehetbauer, Lattice defect investigation of ECAP-Cu by means of X-ray line profile analysis, calorimetry and electrical resistometry, *Mater. Sci. Eng. A* 410-411 (2005) 169–173.

[32] D. Setman, E. Schäfer, E. Korznikova, M.J. Zehetbauer, The presence and nature of vacancy type defects in nanometals detained by severe plastic deformation, *Mater. Sci. Eng. A* 493 (2008) 116–122.

[33] J. Gubicza, Defect Structure and Properties of Nanomaterials, Woodhead Publishing, Duxford, UK, 2017.

[34] A.A. Popov, I.Y. Pyshmintsev, S.L. Demakov, A.G. Illarionov, T.C. Lowe, A.V. Sergeyeva, R.Z. Valiev, Structural and mechanical properties of nanocrystalline Ti processed by severe deformation processing, *Scripta Mater.* 37 (1997) 1089–1094.

[35] A. Hasnaoui, H. Van Swygenhoven, P.M. Derlet, On non-equilibrium grain boundaries and their effect on thermal and mechanical behaviour: a molecular dynamics computer simulation, *Acta Mater.* 50 (2002) 3927–3939.

[36] N.Q. Vo, J. Schafer, R.S. Averback, K. Albe, Y. Ashkenazy, P. Bellon, Reaching theoretical strengths in nanocrystalline Cu by grain boundary doping, *Scripta Mater.* 65 (2011) 660–663.

[37] J. Gubicza, Annealing-induced hardening in ultrafine-grained and nanocrystalline materials, *Adv. Eng. Mater.* 22 (2020) 1900507.